Journal of Nuclear Materials 377 (2008) 275–284

Contents lists available at ScienceDirect

Journal of Nuclear Materials

journal homepage: www.elsevier.com/locate/jnucmat

Radiation flux and damage at accelerator-driven spallation neutron sources

M.S. Wechsler [a,*,1], W. Lu [b]

[a] Department of Nuclear Engineering, North Carolina State University, Raleigh, NC 27695-7909, USA
[b] Spallation Neutron Source, Oak Ridge National Laboratory, Oak Ridge, TN 37831, USA

ARTICLE INFO

PACS:
24.10.Lx
61.80.−x
61.80.Az
61.80.Bg
61.80.Hg
61.80.Jh

ABSTRACT

Radiation damage (displacement, helium, and hydrogen production) at proton-driven spallation neutron sources is analyzed and compared for SNS SB (316SS at the nose of the Hg-container vessel), SNS PEW (Al6061 at a hypothetical proton entrance window), and SINQ EW (Al–3 wt% Mg entrance window at Target 5). Spallation neutrons at the three components exhibit differential fluxes, ϕ', that increase monotonically with decreasing energy E. For SINQ EW, ϕ' is roughly proportional to 1/E, which is attributed to the moderating effect of the D_2O coolant and moderator tank. For 316SS at SNS SB, the calculated total displacement production rate due to protons and neutrons is 34 dpa/yr at full power, with about 37% due to protons. For the Al at SNS PEW and SINQ EW, however, the total rate is 4–5 dpa/yr, with about 90% due to protons. He and H production in all three components is dominated by the incident protons. For He, comparison of experimental and calculated production cross sections for protons on 316SS and Al indicates the need to employ the non-default Jülich ILVDEN option in running LAHET. The resulting total production rates for SNS SB, SNS PEW, and SINQ EW are about 3000, 2400, and 1900 appmHe/yr, respectively. These rates are 1.5–2 times the rates previously calculated using the default GCCI ILVDEN option. The high mobility of H atoms promotes H escape from thin targets of 316SS and Al. For 0.1 cm-thick samples, we tallied the H where it comes to rest using IOPT 14, and obtained production rates at SNS SB, SNS PEW, and SINQ EW of 11500, 4300, and 3500 appmH/yr, respectively.

1. Introduction

Our aim is to analyze and compare calculations of radiation damage (displacements, He, and H production) due to protons and spallation neutrons at two components at SNS and one component at SINQ. The three components are:

(1) SNS SB: This is the 'Smallest Box' at the innermost 316-stainless-steel shell of the nose of the SNS target container module. As described in [1,2], the SNS SB is a 0.1 cm^3 tally volume, 0.13 cm thick, that extends from the outer to the inner surface of the shell. It is in contact with the Hg spallation target material. The SNS SB receives a 2 mA current of 1000 MeV protons with a central incident current density of 1.4×10^{14} protons/cm^2 s.
(2) SNS PEW (Proton Entrance Window): This is a hypothetical Al6061 component (the actual material for the proton entrance window is now taken to be Inconel 718). The SNS PEW lies 2.38 m upstream of the SNS SB. The incident current density of the 1000 MeV protons on the SNS PEW is 1.75×10^{14} protons/cm^2 s [3].
(3) SINQ EW (Entrance Window): The calculations for this component are directed toward Target 5 at SINQ, which receives a beam of 570 MeV protons at a current of 1.1 mA [4–6]. The target vessel is a double-walled structure of an Al-3 wt% Mg alloy designated as AlMg3. The entrance window consists of outer and inner hemispheres, which are connected to mating outer and inner cylinders. The protons are incident on the entrance window from below, and we focus our attention on the inner shell at the centerline lowest point of the hemisphere (see Fig. 6 in [4] or Fig. 1 in [5]). The incident current density at this point is 1.75×10^{14} protons/cm^2 s (coincidentally the same as for SNS PEW). The spallation target material at SINQ Target 5 is Pb. SINQ EW is separated from the nearest Pb spallation target rod by about 15 cm of D_2O coolant.

The three materials (316SS at SNS SB, Al6061 at SNS PEW, and AlMg3 at SINQ EW) receive the maximum proton current density in the incident beams. The nominal composition for 316SS is Fe + 16–18 wt% Cr + 10–14 wt% Ni. A nominal composition for Al6061 is Al + 1.0 Mg + 0.6 Si + 0.3 Cu + 0.2 Cr (in wt%) [3], and for AlMg3 it is Al + 2.7 Mg + 0.35 Mn + 0.30 Si + 0.25 Fe (in wt%)

* Corresponding author. Tel./fax: +1 919 929 5193.
E-mail address: wechsler@ncsu.edu (M.S. Wechsler).
[1] Present address: 322 Carolina Meadows Villa, Chapel Hill, NC 27517, USA.

0022-3115/$ - see front matter © 2008 Elsevier B.V. All rights reserved.
doi:10.1016/j.jnucmat.2008.02.089

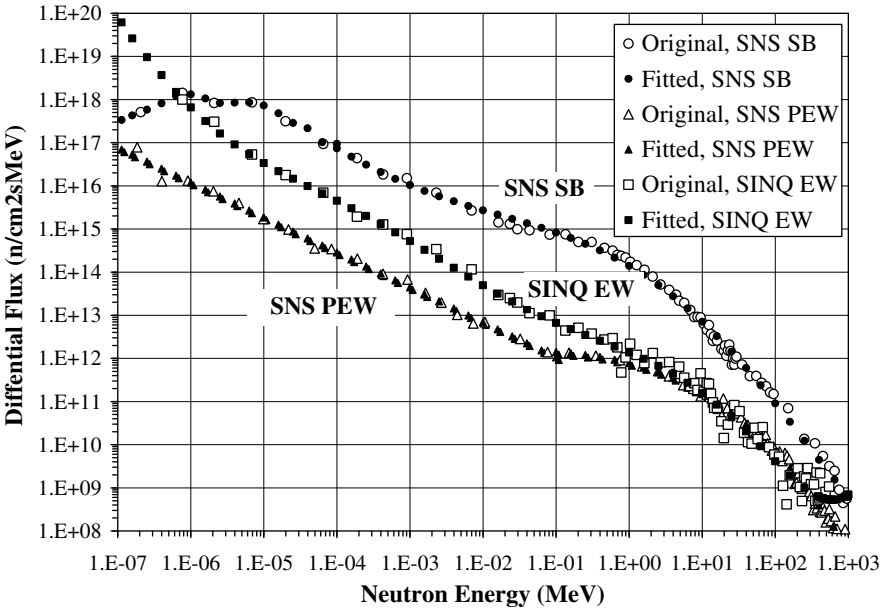

Fig. 1. Differential flux vs neutron energy for SNS SB, SNS PEW, and SINQ EW. Open symbols, original calculated points; filled symbols, fitted points.

[7]. Damage cross sections for the two Al alloys will differ only slightly from those for pure Al, and we refer to the two materials simply as 'aluminum'.

2. Proton and neutron fluxes

As mentioned above, the proton current densities for SNS SB, SNS PEW, and SINQ EW are 1.4, 1.75, and 1.75, respectively, in units of 10^{14} protons/cm^2 s at energies of 1000, 1000, and 570 MeV, respectively. Since the protons are directly incident on the target metal, there is only a slight admixture of lower energy protons in the proton flux. For the 316SS at SNS SB, about 92% of the displacement-producing protons have energies above 900 MeV, and the proton flux of all energies is about 8.5% greater than the incident current density, which is attributed to the secondary protons [1]. Similarly, for the aluminum at SINQ EW more than 98% of the protons in the flux at the center of the entrance window have energies between 569 and 570 MeV [5], and the proton flux of all energies is about 4.6% greater than the incident current density, due to the secondary protons [4]. Thus, we may neglect the relatively small damage contribution due to secondary protons, as was done for SNS PEW in [3].

In contrast to the proton flux, the neutron flux spectra are distributed over a wide range of energies. Fig. 1 shows the differential neutron flux for SNS SB, SNS PEW, and SINQ EW over the full neutron energy range above 10^{-7} MeV. Except for the SNS SB region below 10^{-6} MeV, the differential neutron flux increases with decreasing neutron energy. These neutron spectra are quite different from the accustomed prompt fission spectra in nuclear reactors, as can be seen in Fig. 2 by comparing the SNS SB and prompt fission curves, corresponding to the same total neutron flux of all energies of 8×10^{14} n/cm^2 s. For the fission flux, we used the expression determined by Cranberg et al. [8] for the differential U-235 fission neutron number density.

$$N'(E) = N(0)\frac{2a}{\sqrt{\pi}}(aE)^{1/2}\exp(-aE) \tag{1}$$

where $a = 0.775$ MeV^{-1}. $N(0)$ is the number of neutrons per unit volume of all energies. The differential fission flux is then given by

$$\phi'(E) = vN'(E) = \left(\frac{2E}{m}\right)^{1/2} N'(E) = BE\exp(-aE) \tag{2}$$

where v is the neutron velocity, m is the neutron mass, and B is a constant. Integrating (2) over all energies, we find that the flux of neutrons of all energies = $\phi(0) = B/a^2$, whereby

$$\phi'(E) = \phi(0)a^2E\exp(-aE) \tag{3}$$

The most probable neutron energy in this flux spectrum is $1/a = 1.3$ MeV and the average energy is $2/a = 2.6$ MeV. We see in Fig. 2 that the differential neutron fluxes for SNS SB and prompt fission are in rough agreement only for neutrons with energies between about 1 and 10 MeV. As the neutron energy decreases below 1 MeV and increases above 10 MeV, the SNS SB differential flux becomes increasingly much higher than for prompt fission.

The moderated flux curve in Fig. 2 is based on the analysis of the slowing down of neutrons for fission reactors (see, for example, [9], Chapter 3), which indicates that, depending upon considerations such as source parameters and the degree of neutron absorption or escape, the differential neutron flux for the slowing-down energy range may be approximated by

$$\phi'(E) = \frac{\phi_0}{E} \tag{4}$$

where ϕ_0 is a constant flux value. The total moderated flux of neutrons from $E_1 = 10^{-7}$ MeV to $E_2 = 1000$ MeV is therefore

$$\phi(E_1, E_2) = \phi_0 \ln\left(\frac{E_2}{E_1}\right) = 23.0\phi_0 \tag{5}$$

and ϕ_0 for the moderated flux curve in Fig. 2 is equal to 3.58×10^{13} n/cm^2 s, consistent with the same total flux of 8.2×10^{14} n/cm^2 s as for SNS SB. It is clear in Fig. 2 that the differential flux for SNS SB is much better approximated by the moderated flux curve than the prompt fission flux curve. It follows from Eq. (4), that the average energy, <E>, in the moderated flux over energy range (E_1,E_2) is given by

$$\langle E\rangle = \frac{E_2 - E_1}{\ln(\frac{E_2}{E_1})}. \tag{6}$$

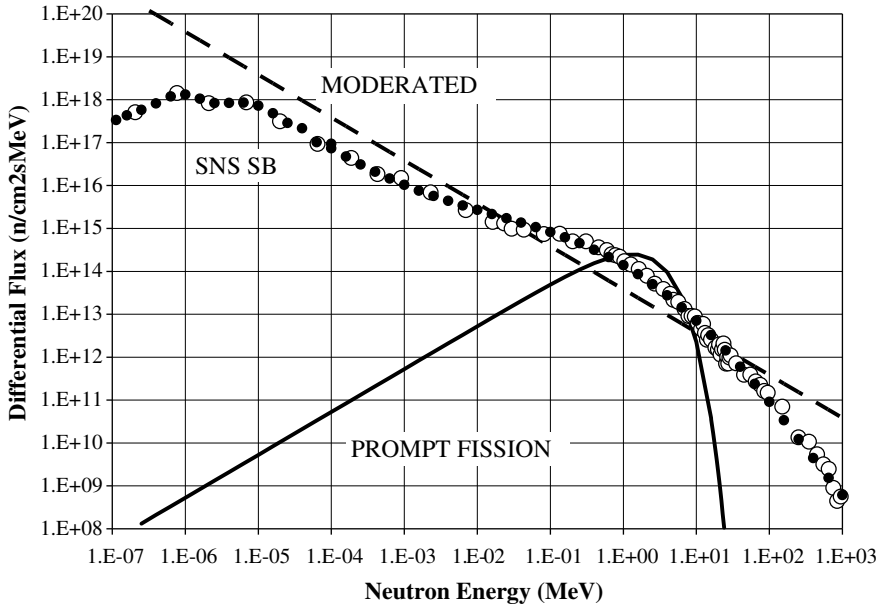

Fig. 2. Differential flux vs neutron energy for SNS SB, fission spectrum, and moderated spectrum. The total neutron flux of all energies is the same for all three curves, i.e., the total neutron flux for SNS SB, 8E14 n/cm^2 s.

Also, the fractional flux with energies between E_1 and E is

$$f(E_1, E) = \frac{\ln(\frac{E}{E_1})}{\ln(\frac{E_2}{E_1})} \tag{7}$$

Fig. 3 shows the cumulative flux (flux due to neutrons with energies below E versus neutron energy E). As noted in Fig. 3, the total neutron flux of all energies above 10^{-7} MeV for SNS SB, SNS PEW, and SINQ EW are 8, 0.08, and 0.2, respectively in units of 10^{14} n/cm^2 s. These relative total neutron fluxes may seem surprising in view of the incident proton current densities of 1.4, 1.75, and 1.75, respectively, in units of 10^{14} protons/cm^2 s. However, the geometries of the three components are quite different. In particular, for SNS SB the 316SS is in direct contact with the Hg spallation source, for SNS PEW the Al is about 2.4 m upstream of the nearest Hg spallation source material, and for SINQ EW the Al is about 15 cm from the nearest Pb spallation target rod.

In part (A) of Table 1, several energy spectrum quantities are presented, as derived from the neutron flux data for energies above 10^{-7} MeV shown in Figs. 1–3 for the five cases considered there. Although in principle the neutron energies extend up to 1000 MeV for SNS SB and SNS PEW and up to 570 MeV for SINQ EW, the average energies for these three spallation cases are only 5.7, 31, and 23 MeV, respectively, as compared to 2.6 MeV for the fission spectrum and 43 MeV for the moderated spectrum (Eq. (6)) over energy range $(E_1, E_2) = (10^{-7}, 1000)$ MeV or 25 MeV over

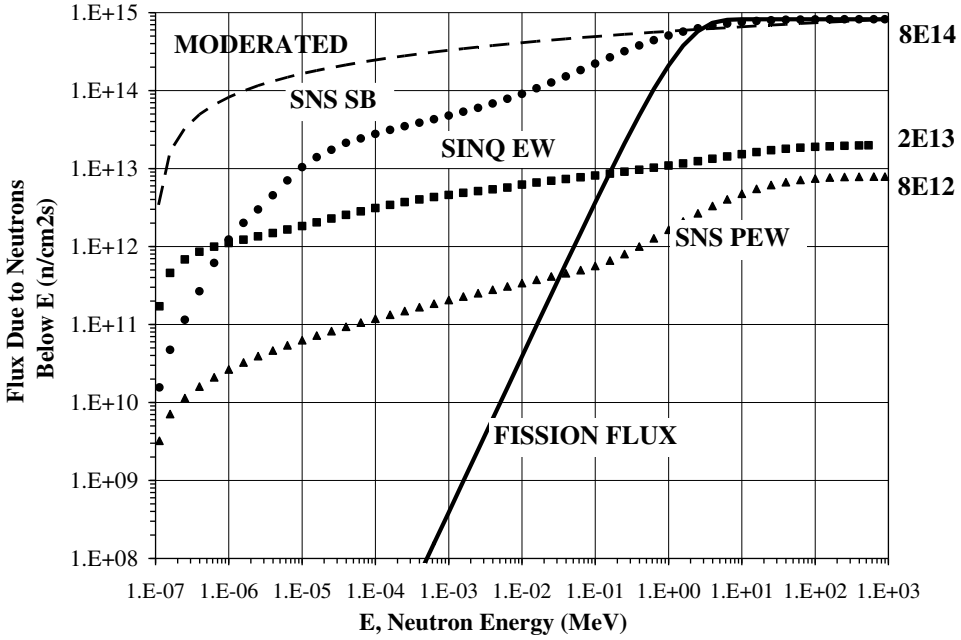

Fig. 3. Neutron flux due to neutrons with energies below E vs neutron energy E for SNS SB, SNS PEW, and SINQ EW; fitted points. Curves are also shown for moderated fluxes for energies E_1 = 0.1 eV to E_2 = 1000 MeV and for prompt fission flux with the same total flux as SNS SB.

Table 1
Energy spectrum quantities for neutrons in the flux and for neutrons producing displacements, He, and H for 316SS in fission and moderated neutron spectra, 316SS at SNS tally volume SB, Al6061 at SNS PEW proton entrance window and AlMg3 at SINQ EW Target 5 inner entrance window

(1) Case	(2) Average energy (MeV)	(3) Median energy (MeV)	(4) Central 90% energy range (MeV)[a]
(A) Flux			
Fission	2.6	2.2	0.46–6.1
Moderated	43	0.01	3.2E−7 to 320
SNS SB	5.7	0.52	0.00053–17
SNS PEW	31	6.0	0.021–110
SINQ EW	23	0.51	6.4E−7 to 97
(B) Displacements			
Fission	3.4	3.6	0.78–6.7
Moderated	150	37	0.88–680
SNS SB	19	4.8	0.28–55
SNS PEW	26	10	0.62–71
SINQ EW	24	5.6	0.073–81
(C) Helium			
Fission	6.7	6.0	2.8–10
Moderated	400	310	13–840
SNS SB	63	17	4.9–217
SNS PEW	98	35	8.9–420
SINQ EW	97	39	8.8–390
(D) Hydrogen[b]			
Fission	5.1	4.2	1.9–8.5
Moderated	300	130	15–800
SNS SB	60	23	3.6–160
SNS PEW	94	40	8.1–370
SINQ EW	70	33	7.3–270

[a] Central 90% energy range E_1–E_2: E_1 and E_2 are energies below which the fractional flux (in the range from 1E−7 to 1000 MeV) is less than 0.05 and above which the fraction flux is greater than 0.95, respectively.

[b] For $E \leqslant 150$ MeV, H cross sections are based on LA150. For $E > 150$ MeV, they are based on LAHET with IOPT14 (tallied where the H comes to rest) and GCCI with MPM on.

$(10^{-7},570)$ MeV. The median energies for fission flux, moderated flux, SNS SB, SNS PEW, and SINQ EW are all lower than the corresponding average energy. The average-to-median energy ratios for SNS SB, SNS PEW, and SINQ EW are 11, 5.1, and 45, respectively, while for the fission flux it is only 1.2. The larger values of this ratio for the spallation cases (and especially for SINQ EW) than for the fission flux are a reflection of the greater neutron moderation. The particularly strong neutron moderation for SINQ EW is also seen in column (4) of part (A) in Table 1 in that the central 90% energy range extends all the way from 6×10^{-7} to 97 MeV. A reason for strong moderation at SINQ EW may be the presence of the deuterium in the D_2O coolant and in the surrounding moderator tank. For the fully moderated spectrum, it follows from Eq. (7) that the median energy for neutrons in the energy range from $E_1 = 10^{-7}$ to $E_2 = 1000$ MeV is 0.01 MeV, and the average-to-median energy ratio is 4300. For comparison with SINQ EW, where $E_2 = 570$ MeV, the moderated-flux median energy by Eq. (7) is 0.00755 MeV and the average-to-median energy ratio is 25.4/0.00755 or about 3400. We note that the average energy of 25 MeV for the moderated flux by Eq. (6) agrees with the value of 23 MeV for SINQ EW (Table 1), but the median energy of 0.00755 MeV for the moderated flux by Eq. (7) is considerably lower than the median energy of 0.51 MeV for SINQ EW (Table 1).

Fig. 4 shows the differential flux for SINQ EW as given in Fig. 1 and for the moderated flux as calculated using Eq. (4), where ϕ_0 is given by the average value of the SINQ EW $E\phi'(E)$, equal to 8.75×10^{11} n/cm^2 s. Integrating Eq. (4) over the entire neutron energy range (i.e., from $E_1 = 10^{-7}$ MeV to $E_2 = 570$ MeV), we find that ϕ (total) $= \phi_0 \ln(E_2/E_1) = 1.97 \times 10^{13}$ n/cm^2 s, in agreement with the calculated value for SINQ EW of 2.0×10^{13} n/cm^2 s as shown in Fig. 3. There is in Fig. 4 a negative departure of the differential flux for SINQ EW from the straight line for the moderated spectrum in the neutron energy range from 0.1 to 10 eV. This means that the flux of these low-energy neutrons rises more rapidly for the moderated spectrum than for SINQ EW, resulting in a lower median energy for the moderated flux.

3. Displacement production

The 316SS and Al cross sections used for the calculation of displacement production are shown in Fig. 5. Several cross-section sources were used, depending on the proton and neutron energies: for $E < 20$ MeV, SPECTER [10] and ENDF [11]; for $20 < E < 150$ MeV, LA150 [12]; and for 150 MeV$<E$, LAHET/MCNPX [13,14]. The

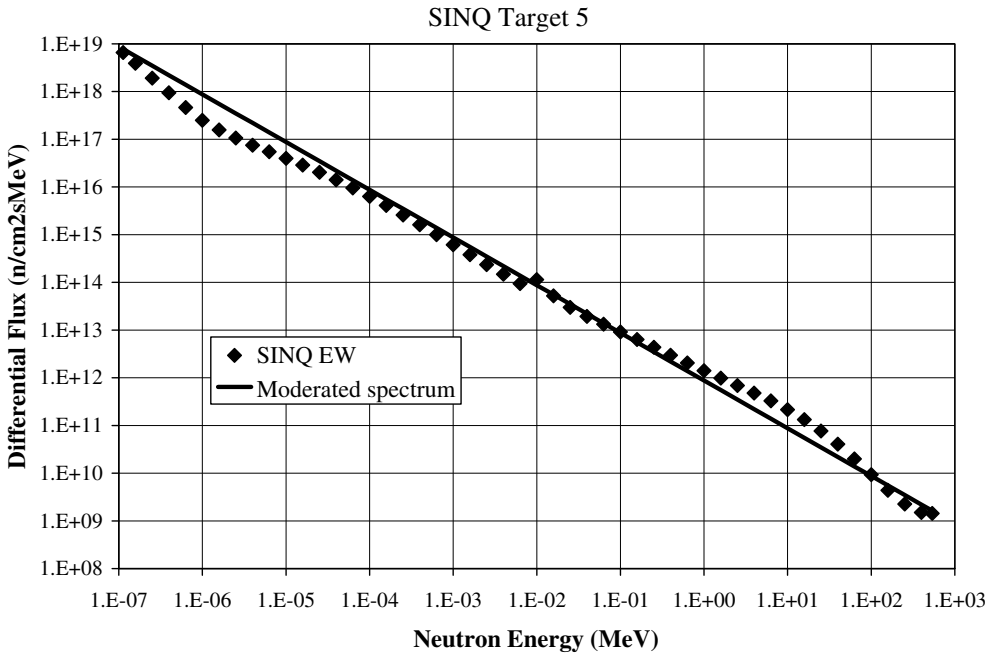

Fig. 4. Differential neutron flux vs neutron energy for SINQ EW over the entire range from $E_1 = 0.1$ eV to $E_2 = 570$ MeV and for the moderated spectrum where $\varphi'(E) = \varphi_0/E$ and $\varphi_0 = 8.75 \times 10^{11}$ n/cm^2 s.

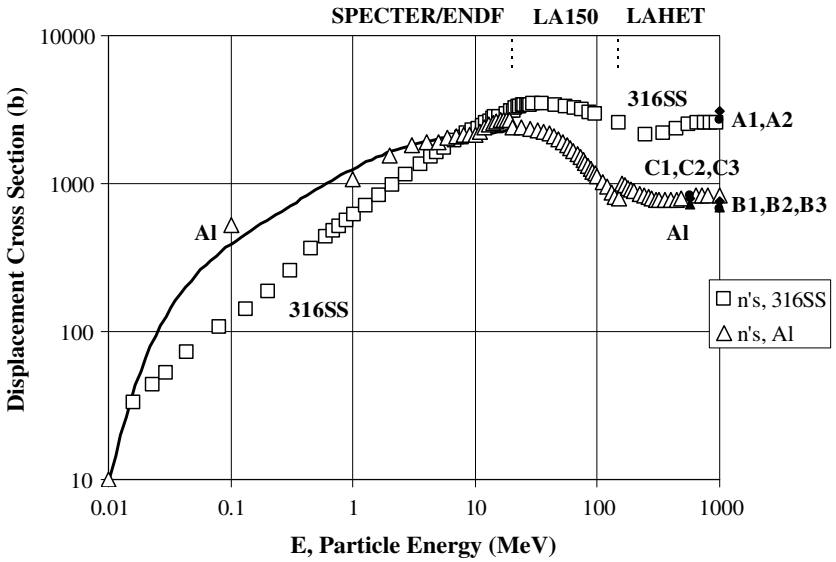

Fig. 5. Displacement cross section versus neutron or proton energy for 316SS and aluminum. Vertical dashed lines at the top border show the ranges for SPECTER or ENDF, LA150, and LAHET. Below 20 MeV, the triangles and squares represent SPECTER calculations and the curve represents ENDF values fitted to a fifth-order polynomial between 0.01 and 20 MeV. The filled symbols near A1 and A2 (316SS at 1000 MeV); B1, B2, and B3 (Al at 1000 MeV); and C1, C2, and C3 (Al at 570 MeV) represent cross sections for protons (see Table 2).

demarcations between the three energy regions are shown in Fig. 5 by dashed vertical lines at the top-right border. Also shown in Fig. 5 are a number of smaller filled symbols at 570 and 1000 MeV, representing proton-induced cross-section values, as given in Table 2. These points indicate that the proton and neutron cross sections at these energies are quite similar in value. Within MCNPX, it is possible to select various intranuclear cascade (INC) models, including Bertini and CEM2k [15]. The operative INC and the number of histories are given in Table 2 for each of the proton-cross-section determinations. Cross-section discrepancies between the codes are discussed for Al, Fe, and W in [16]. For Al, the discrepancies are relatively small, particularly above about 100 MeV (Fig. 1 in [16]).

In Table 1(B), the energy spectrum quantities for displacement-producing neutrons are indicated for the five cases, and we see that, except for the average energy for SNS PEW, the average and median energies are increased relative to the corresponding values for the flux in Table 1(A). Also, for displacements in Table 1(B) (as for the flux in Table 1(A)), the average energies are higher than the median energies. In addition, the central 90% energy range in 1(B) is decreased as compared to 1(A), particularly due to a striking increase in the lower bound of the range. This is consistent with the sharp decreases in displacement cross section below about 10 MeV (Fig. 5).

Table 2
Displacement cross section (CS) and production rate (K_d) for protons on 316SS at SNS SB and Al at SNS PEW and SINQ EW (See Fig. 5)

Case	Proton energy (MeV)	CS (b)	K_d[a] (dpa/yr)	INC; no. of histories	Reference
A1, 316SS, SNS SB	1000	2670	11.8	Bertini, 1E5	[1]
A2, 316SS, SNS SB	1000	3120	13.8	CEM2K, 1E5	[4]
B1, Al, SNS PEW	1000	678	3.7	Bertini, 1.5E5	[6]
B2, Al, SNS PEW	1000	759	4.2	Bertini, 1E6	[4]
B3, Al, SNS PEW	1000	693	3.8	CEM2k, 1E5	[4]
C1, Al, SINQ EW	570	825	4.6	Bertini, 1.5E5	[3]
C2, Al, SINQ EW	570	802	4.4	Bertini, 1E6	[4]
C3, Al, SINQ EW	570	726	4.0	CEM2k, 1E5	[4]

[a] Based on incident proton current densities of 1.4, 1.75, and 1.75×10^{14} protons/cm^2 s at SNS SB, SNS PEW, and SINQ EW, respectively.

Displacement production rates, K_d, are obtained by folding the displacement cross sections into the proton and neutron fluxes. For the protons, it is sufficient simply to multiply the displacement cross section for the energy of the incident protons by the incident proton current density. The displacement production rates calculated in this way are given in Tables 2 and 3. We see that the production rate for protons is about 13 dpa/yr for 316SS at SNS SB and about 4 dpa/yr for Al at SNS PEW and SINQ EW. The proton-induced K_d is higher for SNS SB than for SNS PEW (despite the lower incident current density) because of the higher displacement cross section at 1000 MeV for 316SS than for Al). In addition, for protons on Al, K_d is slightly lower for SNS PEW than for SINQ EW because the Al cross section is a little lower at 1000 than at 570 MeV (Fig. 5).

For the neutron-produced displacements, the energy dependence of production rates for 316SS at SNS SB and for the fission and moderated spectra is shown in Fig. 6 and for Al at SNS PEW and SINQ EW in Fig. 7. We see for both 316SS and Al that the displacement-producing neutrons have energies above about 0.1 MeV. It is also evident that the neutrons above about 100 MeV make a minor contribution to displacement production. Thus, the INC-based calculations for neutrons above 150 MeV account for only a few percent of the displacement production, as seen in column (3) of Table 4.

4. Helium production

In running the LAHET code, either as a stand-alone utility or from within MCNPX, the user can implement the default option of a number of parameters or choose one of several alternative options. The nuclear energy-level-density parameter, ILVDEN, is particularly important in this connection, since a number of studies [17–19] have found that LAHET-calculated helium production cross sections are significantly dependent on the chosen option. Three ILVDEN formulations are available: GCCI (default), HETC, and Jülich. In the statistical theory of an excited nucleus, the density of excited levels, 1/D, is given by [[20], Eq. (4.117); [21], Eq. (4.12)]

Table 3
Displacement, He, and H production rates for 316SS in prompt fission flux (FF), moderated flux (MF), and SNS tally volume SB, and for Al at SNS PEW and SINQ EW

			A	B	C	D	E
Case		Energy (MeV)	Displacement rate (dpa/yr)	He rate (appmHe/yr)	H rate[a] (appmH/yr)	He/displacement (appmHe/dpa)	H/He
FF, 316SS	N's	1E−7 to 1000	27	57	480	2.5	8.5
MF, 316SS	N's	1E−7 to 1000	19	780	4400	42	5.6
SNS SB, 316SS							
	N's	1E−7 to 1000	21	220	1500	10	6.9
	P's	1000	12.5	3400[b−] 2600[b+]	9900[c]	270[b−] 210[b+]	2.9[b−] 3.8[b+]
SNS PEW, Al							
	N's	1E−7 to 1000	0.42	16	31	39	1.9
	P's	1000	3.7	2400[c]	4300[d]	650	1.8
SINQ EW, Al							
	N's	1E−7 to 570	0.68	13	80	19	6.0
	P's	570	4.7	1900[c]	3400[d]	410	1.8

Rates refer to beam-on time. Values are rounded off.
[a] H cross sections based on LA150 for $E \leqslant 150$ MeV and on IOPT 14 (H atoms tallied where they come to rest) for $E > 150$ MeV.
[b] As recommended in Table 2 of [19], proton-produced He at SNS SB is based on Jülich formulation for Si, Cr, Mn, and Fe in 316SS (− and + values are for MPM off and on, respectively) and on HETC formulation with MPM off for Mo.
[c] Jülich and MPM-on.
[d] GCCI and MPM-off.

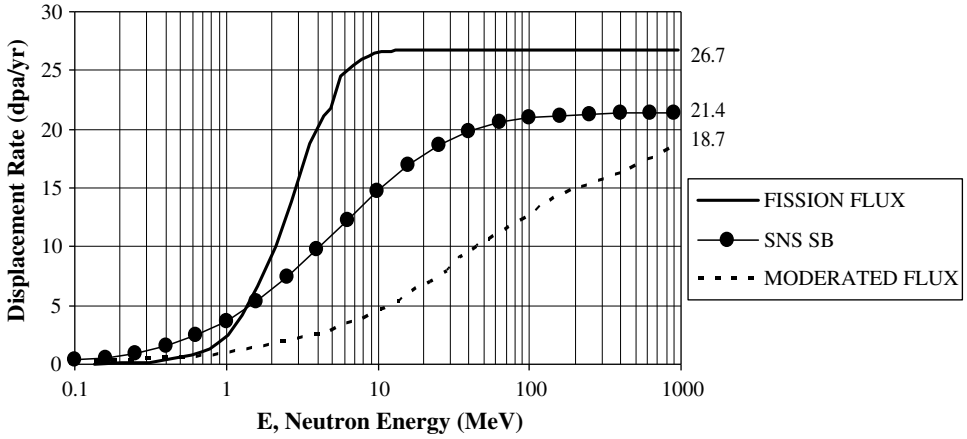

Fig. 6. Cumulative displacement rates (K due to neutrons of energies from 10^{-7} MeV to E) for 316SS at SNS SB vs neutron energy E, using CS's from SPECTER ($E < 20$ MeV), LA150 ($20 < E < 150$ MeV), and Bertini INC within LAHET ($E > 150$ MeV). Curves are also shown for prompt fission flux and moderated flux with the same total neutron flux as for SNS SB.

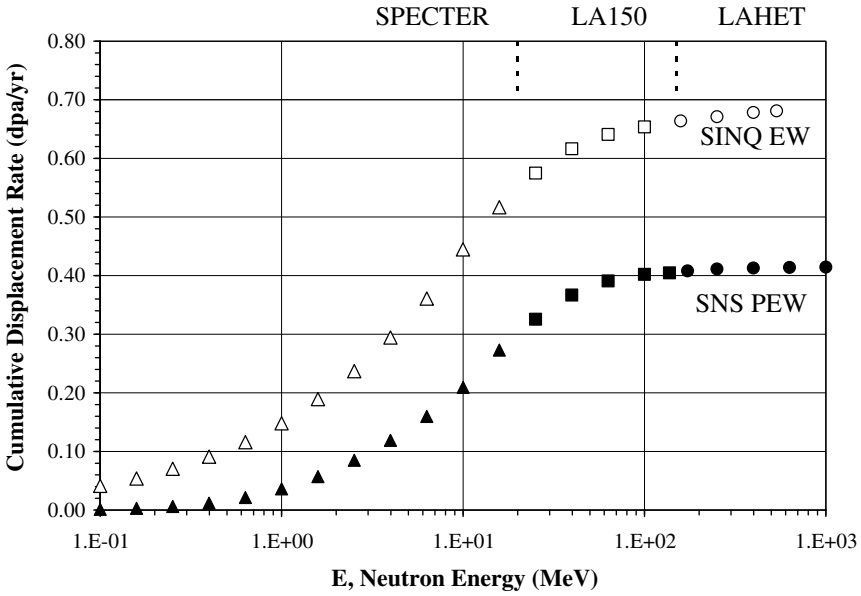

Fig. 7. Displacement rate due to neutrons of energies from 10^{-7} MeV to E vs neutron energy E for SNS PEW and SINQ EW. The cross-section sources are indicated at the upper right border.

Table 4
Percentage contributions by neutrons in three energy ranges to flux, displacements, He, and H at SNS SB tally volume, SNS PEW proton entrance window, and at SINQ EW Target 5 inner entrance window

	(1)	(2)	(3)
Case	E < 20 MeV	20 MeV < E < 150 MeV	150 MeV < E
Neutron flux			
SNS SB	95.6	4.1	0.3
SNS PEW	73	24	3
SINQ EW	84	13	3
Displacements			
SNS SB	83	16	1
SNS PEW	66	32	2
SINQ EW	80	17	3
Helium			
SNS SB	54	39	7
SNS PEW	49	34	17
SINQ EW	33	58	9
Hydrogen			
SNS SB	45	49	6
SNS PEW	19	67	14
SINQ EW	32	59	9

The displacement, He, and H values are based on SPECTER or ENDF, LA150, and Bertini INC CS's, respectively.

$$\frac{1}{D} = C\exp[2(aE)^{1/2}]$$

where E is the excitation energy and C and a are constants. The differences in the three ILVDEN formulations are associated largely with how the constant, a, is expressed [13].

The multistage pre-equilibrium (MPM) parameter, IPREQ, is another option within LAHET that can have an influence on calculated He cross sections. At the end of the INC stage, the nucleus is in an excited state and not yet in the statistical equilibrium appropriate for the evaporation stage. During MPM, the nucleus passes through a series of stages during which particles may be emitted. The net effect of MPM is to drain energy away from He production so that the He cross section is reduced.

Figs. 8 and 9, adapted from [19], show the He production cross sections for protons on Fe and Al, respectively, as calculated using the Bertini and CEM2k INC's and as measured experimentally by a number of authors. A short segment of LA150 results for Al is also shown. Six calculated Bertini curves are included, based on the six

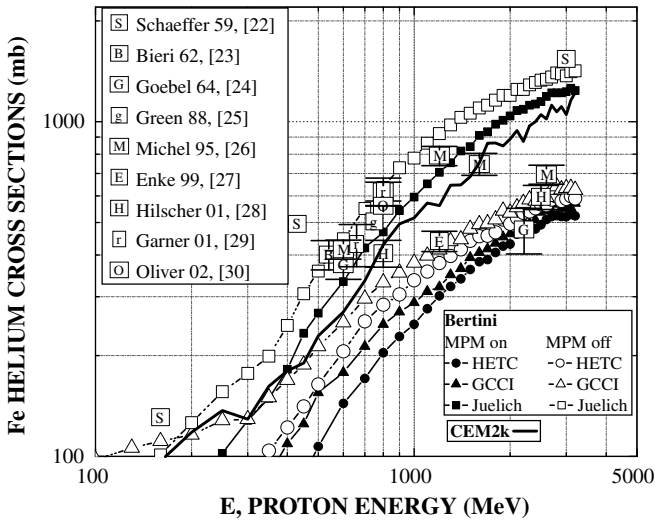

Fig. 8. Helium cross section for protons on Fe ([29], 316SS) vs proton energy, as calculated using the Bertini and CEM2k INC's (lower right legend) and as measured experimentally (upper left legend) [22–30].

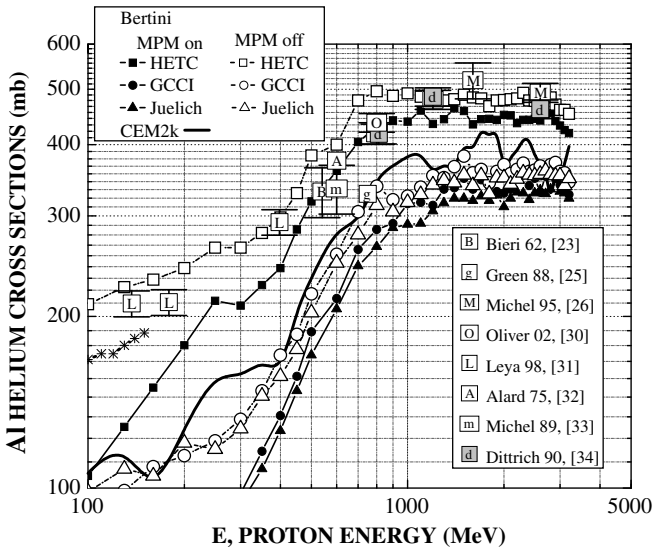

Fig. 9. Helium cross section for protons on Al vs proton energy, as calculated using the Bertini and CEM2k INC's (upper left legend) and as measured experimentally (lower right legend) [23,25,26,30–34]. A short segment from LA150 is also shown.

ILVDEN/IPREQ combinations (ILVDEN with GCCI, HETC, and Jülich formulations and IPREQ with MPM off and on). We see, as mentioned above, that the He cross sections are lower with MPM on than with MPM off. In addition, a number of points (indicated by a single letter within a square box) give experimentally measured cross sections. In the experiments of Oliver et al. [30], the samples were irradiated at 800 MeV at two locations and fluences (high fluence near beam center and low fluence at the edge) at the LANSCE facility. The single points from this experiment in Figs. 8 and 9 stem from the higher fluence irradiation, where there is less influence of spallation neutrons. For Fe, proton irradiated in the 500–1000 MeV range (Fig. 8), the calculated curves using the Bertini INC and the Jülich ILVDEN formulation give best agreement with experiment. The cross sections from MPM on and off, however, seem to agree equally well with experiment, and so it is difficult to recommend a choice for the IPREQ parameter. Thus, in Table 2 of [19], the recommended ILVDEN for Fe is the Jülich formulation, but no choice is made between MPM on and off. This recommendation of the Jülich formulation for Fe agrees with the earlier one in [18], based on comparison of calculations with the experiments using 750 MeV protons by Green et al. [25].

In calculating the He cross section for 316SS, we have used the composition given in [7], namely, in wt%, Fe 65.56, Cr 17.45, Ni 12.2, Mn 1.81, Mo 2.50, and Si 0.39. The NCSU radiation damage database [19] includes 23 elemental targets, which are subdivided into five groups of increasing atomic weight. For the constituents in 316SS, Si is in Group 1 (extending from Mg to Si); Fe, Cr, Ni, and Mn are in Group 2 (extending from Ti to Cu); and Mo is in Group 3 (extending from Zr to Sn). In the recent analysis of He cross sections [19], the recommended ILVDEN options are the Jülich formulation for Groups 1 and 2 and HETC (or GCCI, since its cross sections are close to those from HETC) for Group 3. The information in Fig. 8 for Fe is probably reasonably valid for 316SS also, since the combined effects of Cr and Ni, the major alloying additions, tend to approximate those of Fe. For example, our calculated cross sections for 1000 MeV protons on Fe and 316SS differ by less than two percent. The calculated cross section for 316SS is 0.587 b (with ILVDEN/IPREQ = Jülich/MPM-on) and 0.765 b (with Jülich/MPM-off). A simple average gives 0.676 ± 0.089 b, and the corresponding He production rate due to the incident proton current density of 1.4×10^{14} protons/cm^2 s is about 3000 ± 400 appmHe/yr, as

indicated in Table 3, Column B, for 316SS at SNS SB. The total He production rate due to the spectrum of neutrons, by comparison, is quite low (about 230 appmHe/yr). We see in Table 4 that the fraction of He produced by spallation neutrons above 150 MeV is still quite low, only about 9% (again, based on Jülich/MPM-on options).

With regard to production of He in Al due to protons at SNS PEW and SINQ, there is a difference in the recommended ILVDEN/IPREQ options in the earlier comparison of calculated and experimental He cross sections in [18] (recommending HETC/MPM-on) and the recent comparison in [19] (recommending Jülich/MPM-on or -off). The reason for the change in recommendation is illustrated in Fig. 9. The earlier selection of HETC/MPM-on was based on the measured total cross section of 0.33 b at 750 MeV by Green et al. (Table 2 in [25]), as shown by the experimental point labeled 'g' in Fig. 9. When the additional experimental points are taken into consideration, however, better agreement with experiment for 500–1000 MeV protons is obtained with Jülich/MPM-on. With these selections of the options, the He cross sections for 1000 and 570 MeV protons on Al are 0.44 and 0.35 b, respectively. For the incident current density of 1.75×10^{14} protons/cm^2 s we obtain He production rates of about 2400 and 1900 appmHe/yr for SNS PEW and SINQ EW, respectively, as indicated in Table 3. These proton-produced He rates are about 150 times higher than the neutron-produced rates. The shift from the default GCCI option to the Jülich option produces an increase in the calculated He production of about 50% and 70% at 1000 and 570 MeV, respectively. We note in Table 4 that for Al the percentage contribution to He production by neutrons above 150 MeV is 14 and 9% at SNS PEW and SINQ EW, respectively. Thus, the influence of spallation reactions, while larger than for displacement production, is still rather small for He production.

5. Hydrogen production

A special consideration arises for the high-energy spallation calculation of hydrogen cross sections because of the high mobility of H atoms. In running LAHET, the user is given a choice as to how product atoms are tallied, i.e., the products can be tallied where they are produced (IOPT 3) or where they come to rest (IOPT 14). For a relatively immobile product like He, it does not matter whether IOPT 3 or 14 is used. But, as shown in Fig. 10 for 316SS, IOPT 14 gives lower H cross sections than IOPT 3, indicating considerable leakage of H from the 0.1 cm-thick target. The 0.13 cm thickness for the tally volume for SNS SB was set in accord with the design thickness of the innermost shell at the nose of the SNS target container vessel (although for the initial 316SS target, the thickness is increased from 0.13 to 0.2 cm). The wall thicknesses at SNS PEW and SINQ EW are 0.3 cm [3] and 0.2 cm [7], respectively.

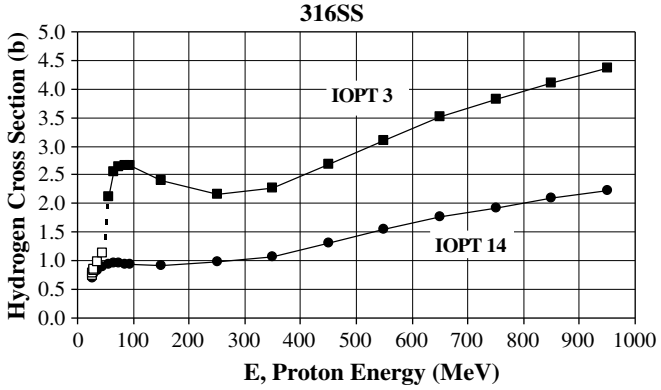

Fig. 10. Hydrogen production cross section versus proton energy for 316SS. The solid squares refer to $E > 50$ MeV and include nuclear elastic scattering. The open squares refer to $E < 50$ MeV and do not include nuclear elastic scattering. LAHET 2.82 with IOPT 3 and 14. GCCI level density formulation and MPM on. Sample thickness 0.1 cm; sample radius 1 cm. On-axis pencil beam. 1E6 incident protons.

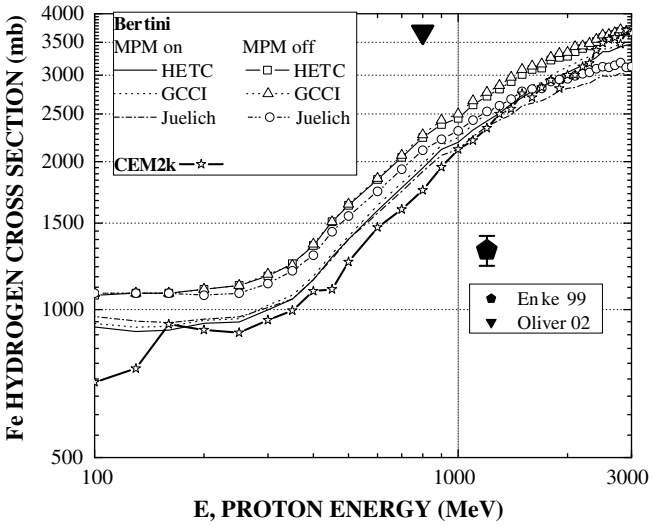

Fig. 11. Hydrogen production cross section vs incident energy for protons on Fe. Experimental points by Oliver et al. [30] and Enke et al. [27]. IOPT 14, thickness 0.1 cm, radius 1 cm, pencil beam, LAHET 2.83, 1 million histories.

Fig. 11 shows H cross sections for protons on Fe, as calculated with the Bertini INC (using IOPT 14 and the various ILVDEN/IPREQ option settings) and the CEM2k INC. Two experimental points are included, but further experimental information is required to determine optimum settings for the calculation. The six Bertini curves are more clustered for H than for He. The Jülich H cross sections are about 10% lower than the GCCI, whereas the Jülich He cross sections are about twice as high as the GCCI, for both MPM on and off as averaged over the proton energy range from 20 to 1000 MeV. In 316SS at SNS SB, H production by protons is greater than by neutrons by a factor of about 6; this factor for He is about 13 (Table 3). Comparing the H cross section for 1000 MeV protons in 316SS (IOPT 14, GCCI/MPM-on, Fig. 10) and in Fe (IOPT 14, GCCI/MPM-on, Fig. 11), we see that they are both about 2.2 or 2.3 b. In addition, there is only a 6% difference at 1000 MeV between the GCCI and Jülich H cross sections. Based on the H cross section for 316SS calculated with the Jülich/MPM-on settings and 1.4×10^{14} protons/cm^2 s for the incident proton flux at SNS SB, the H production rate is calculated to be about 9900 appmH/yr, as shown in Table 3.

Proton ranges in Al are higher than in Fe or 316SS, and again we observe higher H cross sections from IOPT 3 than from IOPT 14, indicating significant leakage of H from 0.1 cm-thick target samples. Based again on IOPT 14, Fig. 12 shows an analogous set of calculated H cross-section curves as for Fe in Fig. 11. For Al, however, there is only one experimental cross-section value, at 800 MeV due to Oliver et al. [30]. This one point agrees best with the calculated curve for GCCI/MPM-off. For these settings and IOPT 14, the H cross sections for protons at 1000 and 570 MeV are 0.77 and 0.62 b, respectively. For the incident current density of 1.75×10^{14} protons/cm^2 s at SNS PEW and SINQ EW, the H production rates are about 4300 and 3400 appmH/yr, respectively (Table 3). The corresponding rates for GCCI/MPM-on would be 4100 and 3200 appmH/yr, respectively. The H production rates for protons on Al at SNS PEW and SINQ EW shown in Table 3 are about 140 and 40 times, respectively, greater than the neutron-produced rates. Table 4 indicates that only about 6% of the neutron-produced H in 316SS at SNS SB is due to neutrons with energies above 150 MeV. For Al at SNS PEW and SINQ EW, the corresponding percentages are 14

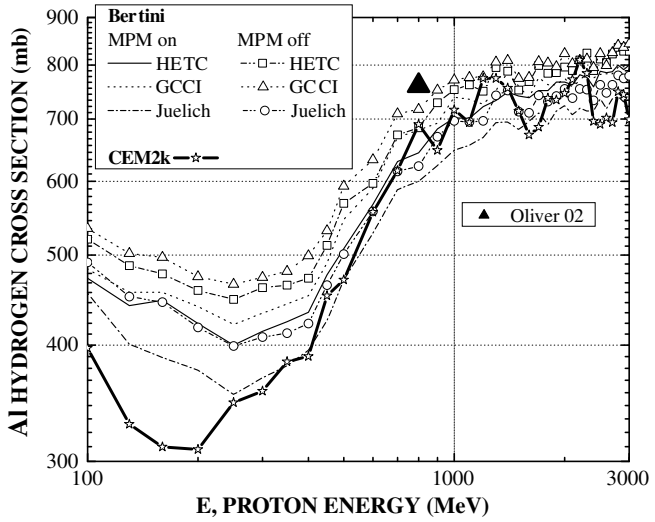

Fig. 12. Hydrogen production cross section vs incident energy for protons on Al. Experimental points by Oliver et al. [30]. Bertini values were obtained using IOPT 14, thickness 0.1 cm, radius 1 cm, pencil beam, LAHET 2.83, 1 million histories.

and 9, respectively. Thus, as was the case for displacements and He, the spallation-calculated cross sections for neutrons play a minor role in calculating H production.

6. Concluding comments

In the previous paragraph, the point was made that calculations based on the physics of spallation reactions may play a minor role in evaluating neutron-produced radiation damage at the three locations, SNS SB, SNS PEW, and SINQ EW, treated in this investigation. It is important to realize from Table 3, however, that damage produced by 570 or 1000 MeV protons is dominant in every instance, except displacement production in the 316SS at SNS SB. For this latter case, almost all of the neutron-produced displacements are due to neutrons with energies below 150 MeV, where spallation reactions become less important. The total calculated displacement damage rate at SNS SB is about 36 dpa per full-power year. At SNS, however, the projected operating schedule calls for about 5000 operating hours/year [3,16], as compared to the full calendar 8760 h/yr. This brings the displacement rate down to about 21 dpa/SNS year. This is still quite a significant damage rate, which can be expected to result in deterioration in mechanical properties. For Al at SNS PEW and SINQ EW, Table 3 indicates more moderate total displacement rates of 4.1 and 5.4 dpa per full-power year, respectively. Since SINQ Target 5 also operates for about 5000 h/yr, the operative rates become 2.3 dpa/SNS year and 3.1 dpa/SINQ year.

It may appear surprising that the neutron-produced displacement rate in 316SS is greater for the fission spectrum (27 dpa/yr) than for SNS SB (21 dpa/yr) for the same total flux (Table 3, column A). But, the flux spectra are quite different for the two cases, and we can see in Fig. 3 and Table 1, column (4), that the relative number of lower energy neutrons is greater for SNS SB. In fact, analysis of the data reveals that the central 90% of displacement-producing neutrons for the fission flux comprise 85% of the total flux, whereas the corresponding fraction for SNS SB is only 56%.

In calculating He production rates at SNS SB, SNS PEW, and SINQ EW, we have attempted to use an increased body of experimental determinations, as a guide in selecting non-default options in the calculations that may be more valid than results from default options. This leads us to the choice of the Jülich ILVDEN option for Group 1 (Mg, Al, and Si) and Group 2 (Ti, V, Cr, Mn, Fe, Co, Ni, and Cu) metals [19]. These targets include all of the non-gaseous constituents of 316SS (except Mo, which accounts for only about 1.5 at.% of the total). Oliver et al. [30] compared experimental and calculated (with default options) He production for their 800-MeV proton irradiations of Al, Fe, Co, Ni, and Cu. Based on the high-fluence data, the experimental-to-calculated He-cross-section ratios are 1.8, 2.2, 2.6, 2.6, and 2.0, respectively, for the five metals. Our calculated Jülich-to-GCCI ratios of He cross sections for 800 MeV protons for the five metals (about the same for MPM on and off) are 1.6, 1.9, 1.9, 1.9, and 1.6, respectively. Thus, it appears that a large part of the calculated underestimates can be removed by shifting from the default GCCI to the Jülich ILVDEN option in running LAHET. The He rate of about 2600 appmHe/yr (Jülich/MPM-on) for 1000 MeV protons on 316SS at SNS SB (Table 3) is about 2.1 times the earlier estimate (Table 2 in [1]) using default GCCI/MPM-on options.

With regard to H production, we have emphasized the important influence of how the H atoms are tallied, i.e., whether they are tallied where they are formed (IOPT 3) or where they come to rest (IOPT 14). Thus, an H atom that is produced within the target, but has sufficient range to be ejected from the target, will be counted in IOPT 3 but not in IOPT 14. It is also true that incident-beam protons that come to rest in the target will be counted as H atoms in IOPT 14, but not in IOPT 3. This is not important here, however, because the ranges of 570- and 1000 MeV protons are so much greater than the 0.1 cm thickness of the targets. Projected ranges as given by SRIM [35] are: 570 MeV protons on Al, 67 cm; 1000 MeV protons on Al and Fe, 152 and 26 cm, respectively. Oliver et al. [30] state that, in the constituents of structural alloys, the protons generated from spallation reactions exist in two roughly equal distributions: the first at energies of about 100 MeV from the INC and the other at about 1 MeV from the later evaporation stage. In Fe at 100 MeV, the projected range of H is about 1.4 cm; at 1 MeV it is 0.00064 cm. We expect, therefore, that most of the H remaining in 0.1 cm-thick Fe targets will have originated from the evaporation stage of the spallation reaction. Oliver et al. also point out that, given the high diffusivity of H in metals, it is perhaps surprising that a large fraction of the H is retained in metals and that trapping of the H at defect clusters and helium sites may play a significant role in H retention. The rapid diffusion of H is likely to be responsible for the observation that differences between measured and calculated H production cross sections may be attributed to the effect of irradiation temperature [36].

It seems clear that further experimental information concerning the formation of He and H at spallation facilities, as well as further refinements in the calculations, are needed in order to obtain a better understanding of how these gaseous elements affect spallation radiation damage.

References

[1] M.H. Barnett, M.S. Wechsler, D.J. Dudziak, L.K. Mansur, B. Murphy, J. Nucl. Mater. 296 (2001) 54.
[2] M.H. Barnett, M.S. Wechsler, D.J. Dudziak, R.K. Corzine, L.A. Charlton, L.K. Mansur, in: Proceedings of the Third International Topical Meeting on Nuclear Applications of Accelerator Technology (AccApp99), American Nuclear Society, La Grange Park, IL, 1999, p. 555.
[3] P.D. Ferguson, M.S. Wechsler, L.K. Mansur, K. Farrell, M.W. Wendel, in: Proceedings of the Accelerator Driven Transmutation Technologies and Applications Meeting (AccApp/ADTTA '01), Reno, Nevada, November 1–15, 2001. Published as a CD by American Nuclear Society, ANS Order Number 700292, ISBN: 0-89448-666-7, 2002.
[4] W. Lu, M.S. Wechsler, Y. Dai, J. Nucl. Mater. 356 (2006) 280.
[5] W. Lu, M.S. Wechsler, Y. Dai, in: Proceedings of the Sixth International Meeting on Nuclear Applications of Accelerator Technology (AccApp'03), American Nuclear Society, La Grange Park, IL 60526, 2004, p. 438.
[6] W. Lu, M.S. Wechsler, Y. Dai, J. Nucl. Mater. 318 (2003) 176.
[7] W. Lu, M.S. Wechsler, Y. Dai, Preliminary Report on Calculation of Radiation Damage to SINQ Target 5 (STIP III), TM-34-03-03, Paul Scherrer Institute, 5232 Villigen PSI, Switzerland, 2003.

[8] L. Cranberg, G. Frye, N. Nereson, L. Rosen, Phys. Rev. 103 (1956) 662.
[9] S. Glasstone, A. Sesonske, Nuclear Reactor Engineering, Van Nostrand Reinhold, NY, 1967.
[10] L.R. Greenwood, R.K. Smither, SPECTER: Neutron Damage Calculations for Materials Irradiations, ANL/FPP/TM-197, Argonne National Laboratory, Argonne, IL 60439, 1985.
[11] V. McLane, (Ed.), ENDF-102, Data Formats and Procedures for the Evaluated Nuclear Data File ENDF-6, BNL-NCS-44945-01/04-Rev., National Nuclear Data Center, Brookhaven National Laboratory, Upton, NY, 2001. See also, http://www.nndc.bnl.gov regarding ENDF-7.
[12] M.B. Chadwick, P.G. Young, S. Chiba, S.C. Frankle, G.M. Hale, H.G. Hughes, A.J. Koning, R.C. Little, R.E. MacFarlane, R.E. Prael, L.S. Waters, Cross-section evaluations to 150 MeV for accelerator-driven systems and implementation in MCNPX, Nucl. Sci. Eng. 31 (1999) 293. See also, LA-UR-98-1825, Los Alamos National Laboratory, 1998.
[13] L.S. Waters, MCNPX User's Manual, Version 2.3.0, Report LA-UR-02-2607, Los Alamos National Laboratory, Los Alamos, NM, 2002.
[14] R.E. Prael, H. Lichtenstein, User Guide to LCS: The LAHET Code System, LA-UR 89-3014, Radiation Transport Group, Los Alamos National Laboratory, Los Alamos, NM, September 1989.
[15] S.G. Mashnik, A.J. Sierk, O. Bersillon, T. Gabriel, Nucl. Instrum. Meth. A414 (68) (1998). Also, Report LA-UR-97-2905, Los Alamos National Laboratory, Los Alamos, NM, 1997.
[16] W. Lu, M.S. Wechsler, P.D. Ferguson, E.J. Pitcher, J. ASTM Int. 3 (7) (2006) Paper JAI13467.
[17] R.K. Corzine, D.J. Dudziak, M.S. Wechsler, M.H. Barnett, L.K. Mansur, Trans. ANS 78 (1998) 289.
[18] L.A. Charlton, L.K. Mansur, M.H. Barnett, R.K. Corzine, D.J. Dudziak, M.S. Wechsler, in: Proceedings of the Second International Topical Meeting on Nuclear Applications of Accelerator Technology (AccApp'98), American Nuclear Society, La Grange Park, IL 60526, 1998, p. 247.
[19] W. Lu, M.S. Wechsler, J. Nucl. Mater. 361 (2007) 282.
[20] G.R. Satchler, Introduction to Nuclear Reactions, Oxford University, NY, 1990.
[21] R.E. Evans, The Atomic Nucleus, McGraw-Hill Book Company, NY, 1955.
[22] O.A. Schaeffer, J. Zähringer, Phys. Rev. 113 (2) (1959) 674.
[23] R.H. Bieri, W. Rutsch, Helvetica Physica Acta 35 (1962) 553.
[24] K. Goebel, H. Schultes, J. Zahringer, Production cross sections of tritium and rare gases in various target elements, Report CERN, 64 (12) (1964) 176p.
[25] S.L. Green, W.V. Green, F.H. Hegedus, M. Victoria, W.F. Sommer, B.M. Oliver, J. Nucl. Mater. 155–157 (1988) 1350.
[26] R. Michel, M. Gloris, H.-J. Lange, I. Leya, M. Lüpke, U. Herpers, B. Dittrich-Hannen, R. Rösel, Th. Schiekel, D. Filges, P. Dragovitsch, M. Suter, H.-J. Hofmann, W. Wölfli, P.W. Kubik, H. Baur, R. Wieler, Nucl. Instrum. Meth. Phys. Res. B 103 (1995) 183.
[27] M. Enke, C.M. Herbach, D. Hilscher, U. Jahnke, O. Schapiro, A. Letourneau, J. Galin, F. Goldenbaum, B. Lott, A. Péghaire, D. Filges, R.D. Neef, K. Nünighoff, N. Paul, H. Schaal, G. Sterzenbach, A. Tietze, L. Pienkowski, Nucl. Phys. A 657 (1999) 317.
[28] Hilscher, C.M. Herbach, U. Jahnke, V. Tischenko, M. Enke, D. Filges, F. Goldenbaum, R.D. Neef, K. Nuenighoff, N. Paul, H. Schaal, G. Sterzenbach, A. Letourneau, A. Böhm, J. Galin, B. Lott, A. Péghaire, L. Pienkowski, J. Nucl. Mater. 296 (2001) 83.
[29] F.A. Garner, B.M. Oliver, L.R. Greenwood, M.R. James, P.D. Ferguson, S.A. Maloy, W.F. Sommer, J. Nucl. Mater. 296 (2001) 66.
[30] B.M. Oliver, M.R. James, G.A. Garner, S.A. Maloy, J. Nucl. Mater. 307–311 (2002) 1471.
[31] I. Leya, H. Busemann, H. Baur, R. Wieler, M. Gloris, S. Neumann, R. Michel, F. Sudbrock, U. Herpers, Nucl. Instrum. Meth. B145 (1998) 449.
[32] J.P. Alard, A. Baldit, R. Brun, J.P. Costilhes, J. Dhermain, J. Fargeix, L. Fraysse, J. Pellet, G. Roche, J.C. Tamain, Nuovo Cimento A30 (1975) 320.
[33] R. Michel, F. Peiffer, S. Theis, F. Begemann, H. Weber, P. Signer, R. Wieler, P. Cloth, P. Dragovitsch, D. Filges, P. Englert, Nucl. Instrum. Meth. B42 (1989) 76.
[34] B. Dittrich, U. Herpers, R. Bodemann, M. Lupke, R. Michel, P. Signer, R. Wieler, H. Hofmann, W. Woelfli, Nuclear Energy Agency Nuclear Data Committee Report (E)-312-U (1990) 53.
[35] J.F. Ziegler, J.P. Biersack, U. Littmark, The Stopping and Range of Ions in Solids, Pergamon, NY, 1985. See also, www.srim.org.
[36] Y. Dai, Y. Foucher, M.R. James, B.M. Oliver, J. Nucl. Mater. 318 (2003) 167.